thermal mass. This stage is illustrated in figure 2(b). For low-Q_0 cases, Kelvin-Helmholtz billows can occur on the interface between the thermal fluid and the stratified-layer fluid; however, apart from these cases, no mixing of the thermal fluid and enveloping stratified-layer fluid can be observed. Figure 3(b) shows some billows above the thermal mass. A thin trail of thermal fluid leaks out along the floor from the rear of the IPF. Apart from this trail, the thermal mass is encapsulated within the IPF and moves with it, as illustrated in figures 2(c) and 3(c). The leakage of fluid in the trail is consistent with the field observations of Doviak and Ge (1984), as interpreted by Doviak et al (1991). Similar leakage was also observed by Maxworthy (1980) in the laboratory.

By about $x = 20$–30, a reduction of the size of the thermal mass inside the IPF can be observed, owing to the loss of mass to the trail behind the IPF. However, while the amplitude of the IPF does reduce throughout this time, the loss in IPF amplitude is not as great as the reduction in its encapsulated thermal mass. This will be discussed in §5. The thermal mass appears in shadowgraph visualizations to be mixed, but by this stage turbulent motions within it seem to have substantially ceased. The fluid in the thermal mass appears virtually motionless on a frame of reference moving with the IPF and does not possess any discernible net circulation or relative vorticity. This stage is shown in figures 3(c) and (d) and diagrammatically in figure 2(d). Transport of substantial mass in the IPF occurs over a distance typically 10 times the horizontal length scale of the IPF. Small-amplitude waves should only transport substantial mass at their propagation speeds over scales comparable with one wavelength.

Eventually the thermal mass will disappear entirely, although the time at which this occurs depends on the parameters. When this occurs, the IPF has degenerated to a phenomenon that could be described as a weakly-nonlinear, small-amplitude solitary wave. It will continue to propagate until it is reflected from the tank end-walls.

In general, the speed of the phenomenon decreases as it travels; in the following, the average speed over the first 40 non-dimensional units in x (80 cm) will be used. The averaging distance is governed by the length of the tank. This averaging removes the x-dependence in the data, allowing comparison with (7) and (6). Averaging was also attempted over shorter, consecutive intervals. However, measurements were not sufficiently accurate to clarify the functional form of the evolution of speed with distance. In some instances, the reduction of speed was not monotonic – it seemed to decrease, increase slightly, then decrease further.

For initial thermal buoyancies sufficient to generate a wave or IPF, the average propagation speeds were all in the range 1.4–2.5 cm s^{-1}. The linear wave speed c_0 given by (3) for BDO (deep-water) boundary conditions is typically 1.5 cm s^{-1} while KdV (rigid-lid) boundary conditions give one-half of this or 0.75 cm s^{-1}. Hence KdV boundary conditions are much less appropriate than the deep-water BDO conditions. This is seen as partial confirmation that the upper layer depth of 10 non-dimensional units (20 cm) was adequate to place the experiments in the deep-water regime. As an additional check, a set of experiments was repeated with a non-dimensional upper-layer depth of 20 (40 cm). These data match the results with an upper layer depth of 10, as shown on figure 4, which will be discussed next. This is consistent with Tung et al (1982) who found that numerical results became similar for dimensionless depths greater than 10. Thus the results are applicable to processes in the oceanic thermocline or in the lower atmosphere that are generated by isolated dense fluid masses.

As noted in §3.2, dimensional analysis based on the observed propagation speed is a way of interpreting the flow evolution. A plot of $c/(NL)$ versus N^2H^3/Q_0 is shown in figure 4, consistent with (7). Error bars for the data are calculated using the formulae described in

Moffat (1988). The data shown are the average speed over the first 40 units (80 cm).

Several features are clear from figure 4. Firstly, the speed of the disturbance does not collapse with the scaling based on the linear long-wave speed, NL. The results lie either above or below the first-mode linear long-wave speed c_0 calculated using (3), which is shown in nondimensional form by the dashed line. These observations can be attributed to the formation of solitary waves, which would increase c above c_0, or to density-driven or bottom-frictional effects, which may decrease c.

Secondly, the data indicate a substantial dependence on H/L or other factors. (The thermal release cylinder was not properly levelled for some $H/L = 3.75$ runs, resulting in the $H/L = 3.70$ data.) Thirdly, for a given H/L, $c/(NL)$ generally decreases with N^2H^3/Q_0, indicating that c decreases with decreasing energy input to the system; that is, with decreasing total buoyancy supplied, Q_0. In all, figure 4 demonstrates that $c/(NL)$ depends on both H/L and N^2H^3/Q_0, but it fails to illustrate the existence of the regime in which transitions from density-driven to wave-dominated behaviour occur.

Figure 5 illustrates relationship (6). It scales c by the thermal arrival speed at the top of the stratified layer ($\sim (Q_0/H)^{1/2}$). It is evident that below a certain critical value of N^2H^3/Q_0, (about 50 to 80), c^2H/Q_0 is independent of H/L, since data from experiments at quite different H/L collapse onto the same curve. However, figure 5 shows that the flow is strongly dependent on N^2H^3/Q_0, so that stratification plays a key role. It is also striking that it is only below this critical value that the IPF was observed. The experiments beyond the critical value of N^2H^3/Q_0 resulted in a wave travelling ahead of the thermal mass, rather than a transitional regime between density-driven and wave-dominated flows. Thus, the condition for the formation of an

IPF may be stated as $N^2H^3/Q_0 <$ 50 to 80. In this IPF regime the average disturbance speed is independent of H/L.

Measurements were also made of the amplitude of the phenomenon, from the video record. Measurements were made at 10 cm intervals starting at 20 cm, i.e. at $x = 10, 15, 20, 25, 30, 35$ and 40. Amplitude was defined as the maximum displacement of the top of the stratified layer above the undisturbed layer height in front of the phenomenon. Also, the 'incremental speeds' were measured: these were calculated from the time taken to cover each interval of 5 units in x. Owing to large scatter in the data, averaging was necessary. The data were averaged for each H/L value. The result is presented in figure 6, along with the relationship between wave speed and amplitude predicted by the weakly nonlinear theory described by (2). Since the average data inevitably incorporates the density-driven, IPF and weakly-nonlinear wave regimes, it was not possible to make a direct comparison with weakly-nonlinear wave theory.

Weakly nonlinear theory can only reasonably be applied while the small parameter $\bar{a} = a/L$ used in its derivation remains 'small', up to possibly 0.5 (Tung et al 1982), but certainly no greater than 1.0. The results here are beyond the regime where weakly nonlinear theory is probably valid. Uncertainty in the amplitude measurements contributes to the significant scatter, despite averaging. The practical difficulty in producing thermal-generated laboratory IPFs with large and controllable amplitude prevented a large amplitude range from being systematically explored, as Stamp & Jacka (1995) did. Nevertheless, the results indicate that a simple relationship between speed and amplitude, such as that expected on the basis of weakly nonlinear wave theory, cannot be the only factor affecting the results. The 'wavelength' of the phenomenon was also measured, and, while similarly scattered, shows a broad trend of increasing with amplitude.

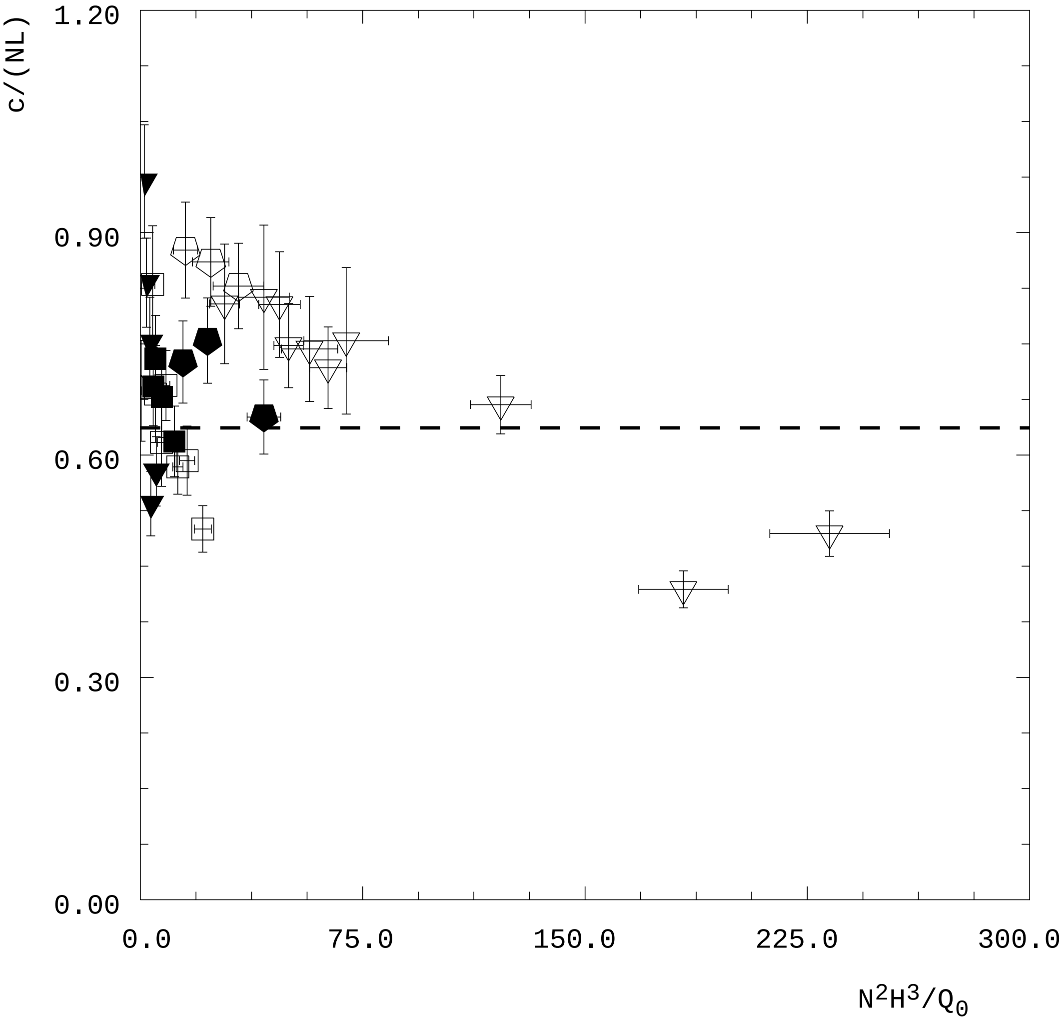

Figure 4: Scaling for wave-dominated physics. Non-dimensional propagation speed $c/(NL)$ over $x = 0$ to $x = 40$ (80 cm), versus the parameter N^2H^3/Q_0. The dashed line is the first-mode linear wave speed corresponding to BDO boundary conditions. The thermal release cylinder was not perfectly level for $H/L = 3.70$ runs.

■ : D/L=20, H/L=2.5; □ : D/L=10, H/L=2.5; and for D/L=10,
▽ : H/L=5.0 ; ⬠ : H/L=3.70; ⬟ : H/L=3.75; ▼ : H/L=1.75.

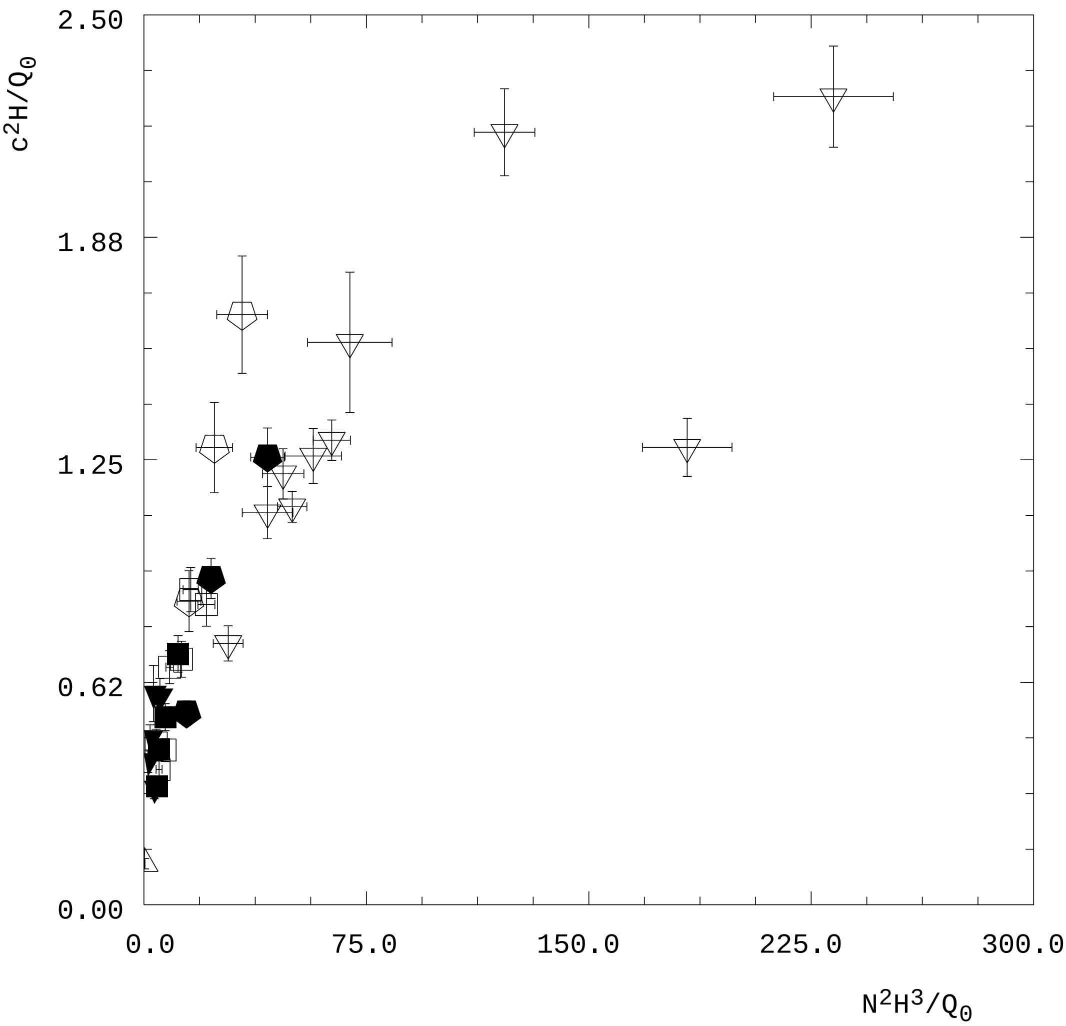

Figure 5: Scaling for density-driven and transitional physics. Non-dimensional propagation speed c^2H/Q_0 over $x = 0$ to $x = 40$ (80 cm), versus the parameter N^2H^3/Q_0; $D/L = 10.0$ for all points. Symbols as figure 4.

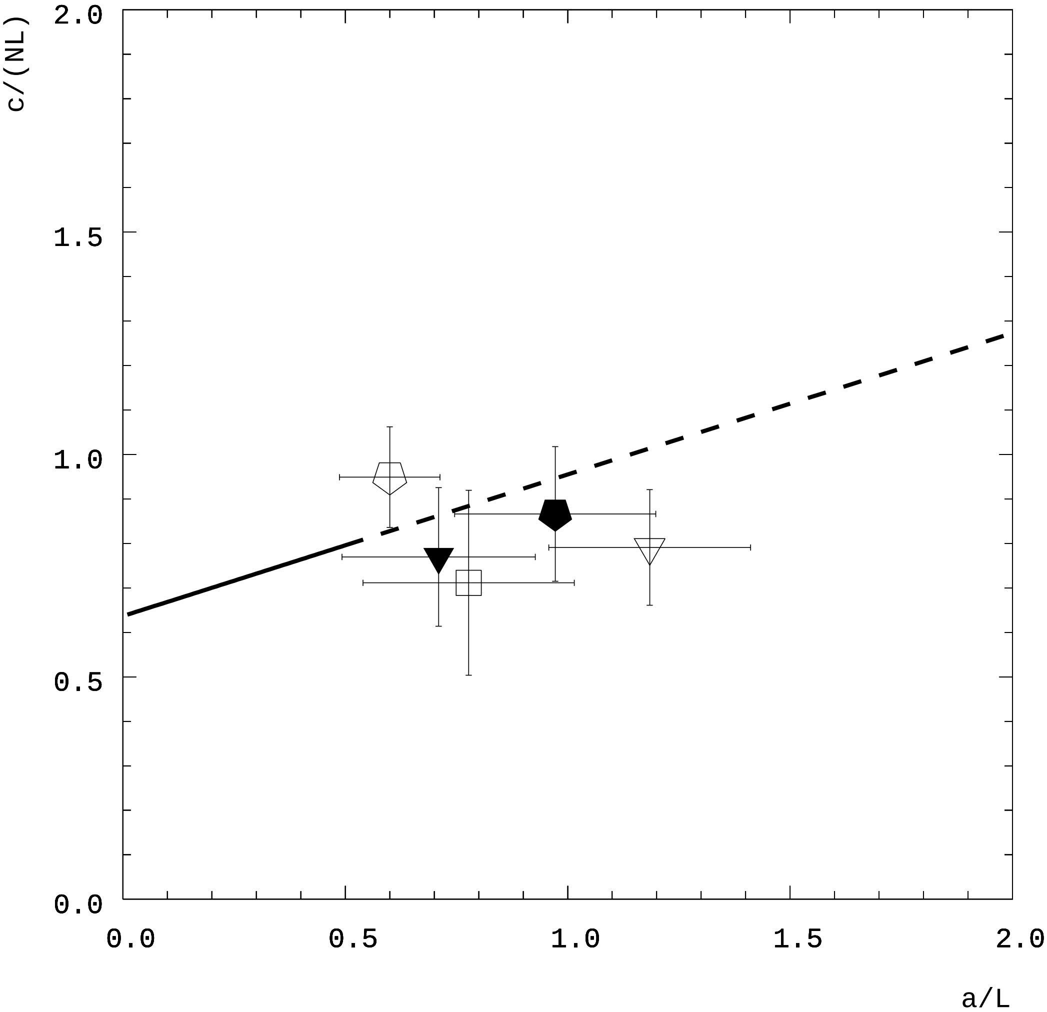

Figure 6: Speed of the phenomenon versus amplitude. These are averages of the incremental speeds over all experiments for each H/L value. Symbols as figure 4; data for $D/L = 10$ and $D/L = 20$ are combined. Error bars are calculated as pooled standard deviations. The solid line up to $a/L = 0.5$ is the relationship predicted by weakly nonlinear theory for a first-vertical-mode soliton; the dashed line is the extrapolation of this relationship beyond the regime where weakly nonlinear theory should be valid. The first-mode linear speed is at $a/L = 0$.

4.2 Vertical structure of the phenomenon - mass transport

The camera was placed at different positions downstream of the release point and the experiment repeated with identical parameters at each position. After a few trials the flows at each position seemed perfectly repeatable. For the particular study to be described below, the parameter N^2H^3/Q_0 was 5.5. This well below the critical value suggested by the results of §4.1, hence an IPF was generated. The parameter H/L was 2.5. The flow evolution revealed by these studies is as follows.

In the first stage, particles in the stratified layer are caught up in the thermal vortex. This stage is shown in figure 7. The data shown covers thirty seconds. Solid lines join the particle images belonging to the same particle. The wave is travelling from left to right across the frame and those particles in orbital paths are rotating counterclockwise. The dominant motion is the positive-vorticity (counterclockwise in figure 7) circulation of the thermal vortex. Particles follow smooth curved paths when caught up in this vortex. The equivalent stage is shown in figure 2(a) and figure 3(a).

Subsequently, the flow begins to translate to the right. Particles are clearly moved right across the image frame. There is still a strong positive vorticity throughout the flow region.

By about $x = 20$, a the flow is in the transitional or IPF regime. This is illustrated in figure 8. This equivalent stage is shown in figure 2(d) and figure 3(c) and (d). The IPF appears to have a dual structure, consisting of a zone of translating mass in the lower portion and a zone of wave activity in the upper portion. The two zones are clearly distinguishable because in the mass-transport zone particles are moved horizontally across the frame with relatively little vertical motion, whilst in the wave-activity zone particles travel on elliptical orbits with no substantial net translation. By 'no substantial' it is